

# ANN-Enhanced Dual Phase Shift PWM Control for Efficient Bidirectional Wireless Power Transfer in Electric Vehicle Applications

Ch.vishnu Chakravarthi <sup>1</sup> (Assistant Professor), Kandipalli vasavi <sup>2</sup>,

B.V.S.S.komalika <sup>3</sup>, Kandregula Harsha ram <sup>4</sup>, Sirasapalli venkata Harish<sup>5</sup>.

DEPARTMENT OF ELECTRICAL AND ELECTRONICS ENGINEERING

SANKETIKA VIDYA PARISHAD ENGINEERING COLLEGE

VISAKHAPATNAM, INDIA.

## ABSTRACT

To support seamless Grid-to-Vehicle (G2V) and Vehicle-to-Grid (V2G) operations, Bidirectional Wireless Power Transfer (BWPT) eliminates manual intervention but faces challenges like power factor control, efficiency, and limited transfer rates. This research proposes a dual-phase shift PWM technique for improved Power Factor Correction (PFC) in BWPT systems. Additionally, an Artificial Neural Network (ANN)-based controller is integrated to enhance dynamic response and optimize switching decisions in real-time. The proposed control strategy is evaluated through simulation and experiments at 85 kHz and 3.7 kW. MATLAB/Simulink is used to model and simulate the BWPT system, enabling detailed performance analysis under various operating conditions. Results show a power transfer efficiency of 94.4% (simulation) and 90.1% (experiment), with improved THD and system robustness. The ANN integration demonstrates strong potential for intelligent, adaptive control in future BWPT systems.

## I. OVERVIEW

The emergence of new energy issues driven by environmental concerns and the depletion of fossil fuels has a substantial impact on the automotive industry. This result has spurred additional research and development in the EV sector [1]. EV recharge is one of the most crucial problems that must be fixed to promote industry growth. Recharge time, safety, and human interaction are the three biggest challenges with EV charging. To get around these problems, the recently created Because WPT technology delivers electricity from a source to a load without making physical touch, it is crucial [2].

WPT provides the user with significantly more comfort and security than traditional wire charging. Since charging cords are no longer necessary thanks to this technology, charging is now safer and more convenient. Because human intervention-free charging capabilities reduce battery size and weight and charging intervals, users can charge smart devices anywhere there is a charging outlet [3]. Additionally, WPT technology finds utility in high-power applications including as railroad traction, underwater vehicles, and wirelessly energizing medical implants [4], [5]. It's not restricted to charging EVs. WPT is important because it may overcome the drawbacks of battery-powered gadgets, namely as limited battery life and high initial costs. WPT's features, such as its dependability, convenience, safety, and weather resistance, have made it more appealing [6]. In particular, it is anticipated that the application of BWPT will hasten the development of V2H, V2V, and V2G technologies, enabling bidirectional electrical flow. The design of the WPT/BWPT systems incorporates completely regulated switching components, such as SIC MOSFETs and IGBTs, allowing high frequency operation for both the primary as well as secondary bridges. Figure 1 displays the standard block diagram that illustrates the interactions between photovoltaic (PV) systems, wirelessly connected EVs, a DC bus, and the power grid in V2G and G2V operations. By improving power quality and grid stability through active or reactive power correction, EVs support the electrical grid [7].

EVs, the power grid, and Renewable Energy Systems (RES) can all be integrated to efficiently boost RES adoption [8]. However, during charging and discharging

conditions, this integration necessitates continuous bidirectional communication.

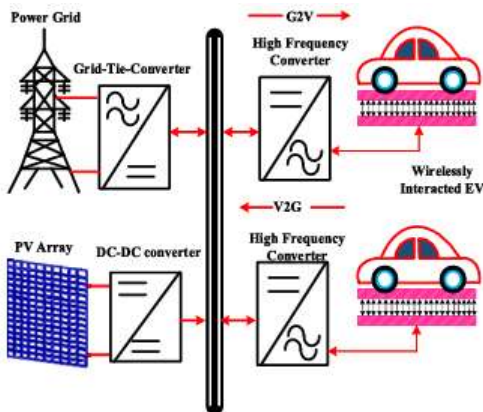


FIGURE 1. Illustration of wirelessly interconnected EVs in the V2G and G2V service.

The grid-connected system must keep the power factor and THD within the permitted range. Additionally, the wireless charging system's power electronic converters are essential to preserving power quality. Misalignment, parameter detuning, coil distance fluctuation, and load variation are some of the uncertain scenarios that cause the WPT system to deviate from its typical behaviour [9]. Additionally, it reduces component stress, power factor, soft switching loss, and power transfer efficiency. However, in order for the BWPT system to preserve grid integration, the power factor is more crucial. Therefore, it is crucial for the wireless charger design to maintain a greater power factor. On the other side, employing appropriate resonance compensation can increase the power transfer efficiency. networks at the primary as well as secondary [10]. To maintain the voltage and current variation, a variety of compensation topologies are suggested for the unidirectional system. Compensating tanks are typically added to the AC links of the two bridges to boost system transmission efficiency and capacity. The symmetrical construction and reduced sensitivity to load variation and coupling coefficient of the LCC-BWPT system have attracted attention [11]. On the primary side, issues brought on by S compensation are mitigated by the LCC compensation architecture [12]. The LCC resonance compensation circuit on the primary side prevents overcurrent issues related to S compensation by using an inverter to convert a voltage source into a current source. This maintains a steady current in the primary coil. Furthermore, even under The LCC resonance correction circuits help to

raise the output voltage under light loads. In conventional BWPT, the direction and amount of actual and reactive power flows are controlled by the relative phase angle and amplitude of the voltages generated by full-bridge inverters on the main and secondary sides [13]. These inverters' switching signals can be synchronized via wireless communication interfaces, however doing so reduces system robustness and increases system costs. By utilizing the active and reactive power of the secondary side's full-bridge inverter for synchronization, an alternative control method eliminates the need for wireless communication [14], [15]. The properties of the passive components and the relative phase angle continue to dictate the real and reactive power flows, as well as the voltage magnitude from the two sides' full-bridge inverters. In wireless circuit designs, recent developments have moved from single-sided to double-sided compensation, offering more flexibility and satisfying WPT system design requirements. [15]

Power regulation from unregulated AC output to regulated DC output is essential for WPT systems running at higher frequencies, particularly when charging EV batteries. To improve system power density in this regard, integrated power factor correction (PFC) circuits have been suggested as an alternative to conventional front-end PFC circuits, which frequently call for large passive components [16]. Although the potential impact on battery life, it is projected that integrating EVs with other resources will benefit grid operators and EV owners monetarily. Power Factor Correction (PFC) has been used to the secondary side of a WPT system in order to increase overall system cost-effectiveness [17]. It's important to recognize, nevertheless, that this method adds more circuit complexity [2]. The importance of the LCCL compensation topology in preserving a steady output voltage on the secondary side is highlighted by the control strategy implemented for the secondary side of a WPT system using an LCCL network. In a similar vein, stability is essential for effectively controlling the linked DC-DC converter that charges batteries [3]. To control A hybrid Inductor Capacitor-Capacitor-Series (LCC-S) compensated technique is used to adjust the output voltage in a WPT system [18]. Phase shift modulation combined with This method, called the LCC-S compensated WPT, enables wide-range output voltage regulation throughout the whole voltage range using a

switch-controlled capacitor [4], [18], and [19]. A 500-W prototype with an input voltage of 400 V and an output voltage of 100-250 V was put together for validation. According to experimental data, the converter achieves a maximum efficiency of 94.1% and maintains Zero Voltage Switching (ZVS) over the voltage range [19]. To generate load-independent Constant Voltage (CV) and Constant Current (CC) outputs at two different sites with zero-phase angular frequencies, a dual-side LCC-LCC compensated WPT converter was thoroughly analyzed [5]. This analysis provided a systematic design strategy. Both weight and Compared to standard WPT topologies, this approach reduces bulk. By utilizing modern Analog Phase Control (APC) and Digital Phase Control (DPC) approaches, the method simplifies its control system by permitting CC and CV power transfer modes [6], [7]. To confirm the accuracy of this innovative method, a combination of simulation analysis and experimental data has been employed. Analyzing secondary active converters as a way to regulate power transfer in WPT systems shows that conventional WPT circuits usually use a front-end PFC interface, leading to large passive components that significantly impact system volume, losses, and dependability. Phase shifts between the primary and secondary sides occur because the primary side lacks intermediary storage elements. Typically, complex synchronization algorithms are used to calculate bridges [7]. For a Full-Bridge Active Rectifier (F-BAR) operating in Bidirectional Wireless Power Transfer (BWPT), a new phase-shift control mechanism was developed. The traditional receiver-side rectifier design has to be altered as a result. Results from simulations and theory demonstrate how this novel control method allows output value control without requiring a transmitter-receiver connection. Maximum efficiency of 94.4% is attained with an output power range of 0 to 3.7 kW and an input voltage of 325V DC. The effectiveness of the converter and suggested control method is confirmed by the experimental validation. The paper's primary contributions include

- Dual-side phase shift-controlled methods enhance the power factor and regulate the power flow.
- The performance study of suggested techniques for the BWPT system, including frequency bifurcation, power loss, and THD.
- The dual side phase shift control method for the BWPT system was validated experimentally and through

Modeling.

While Section III explores alternative BWPT control strategies, with a focus on phase shift control, Section II describes the various BWPT modes of operation. The bidirectional power flow control mechanisms between V2G and G2V are described in Section IV. A 3.7 kW system's design parameters and components are covered in detail in Section V, and an example for assessing the BWPT system's performance in both situations is given in Section VI. The resonant converter incorporates PFC, with one strategy that was put into practice on the primary and secondary sides, respectively. The assessment mostly concentrates on important factors including efficiency, THD, and power losses.

## II. WPT SYSTEM BIDIRECTIONAL

EVs are linked to the DC bus in the BWPT system through the WPT charging mechanism. Coupling coils, high-frequency converters, a compensation circuit, and controllers with specific designs make up each side of the system. The circuit diagram for the suggested topology is shown in Figures 2 and 3 under both charging and discharging circumstances. The primary converter functions as a DC/AC inverter when energy is transferred from the grid to the EV in G2V Mode, and the secondary converter acts as a regulated rectifier for AC/DC conversion. On the other hand, the converters' functions are inverted in V2G mode, when the EV battery feeds electricity to the grid [11]. The circuit consists of an LCC-based resonant converter and a primary side inverter. a converter on the secondary side. In this bidirectional control design, regulation is achieved by matching the duty cycles of the inverters to modify the main side voltage ( $V_p$ ) or secondary end voltage ( $V_s$ ). Power regulation is made possible by varying the average low-frequency signal value of the primary side and secondary end voltages. As previously mentioned, the system consists of both primary and secondary compensation networks.

Through the use of mutual induction principles, which occur during the resonance situation, energy can be transferred from the primary coil to the secondary coil. The controllers play a critical function in overseeing the power transmission between the two coils through out each operational phase.

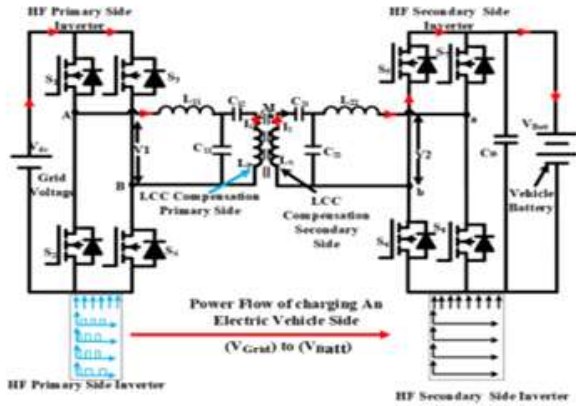


FIGURE 2. BWPT system for the Operation of (VGrid) Side to (VBatt) Side.

An enhanced Pulse Width Modulation (PWM) approach is frequently used for phase shift control, in which control signals are sent to both sides of the converter switches. Fundamental techniques take into account the dual functionality of both primary and secondary converters when implementing bidirectional converters. When the battery receives power from the grid,

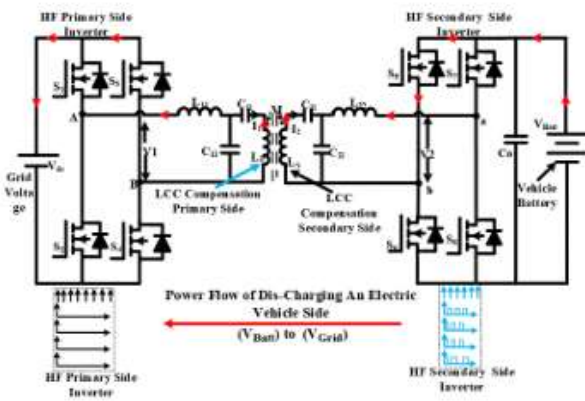


FIGURE 3. BWPT system for the Operation of (VBatt) Side to (VGrid) Side.

The primary converter is controlled by Phase Shifting Modulation (PSM) techniques, while the secondary side converter also serves as a rectifier at the same time. Figure 2 provides an example of this approach. Similarly, the AC/DC converter on the main side acts as a rectifier and the DC/AC converter on the secondary side as an inverter when electricity is transferred from the battery to the grid. Figure 3, which shows the discharge procedure, provides an illustration of this. This approach makes it simple to adjust the active power flow and

calculates the expected efficiency. The power converters must cooperate in order to set up the settings in both controllers. By creating a wireless communication channel, this is accomplished without being constrained by signal processing latency. As a result, both controllers are easily synced and programmable.

**A. BWPT OPERATION MODES Mode I: ( $\alpha$  to  $\pi$ )**

Switches S1 and S4 are conducting on the primary side during the time span  $\alpha$  to  $\pi$ , permitting current to flow through S1, the compensating inductance  $L_{f1}$ , the series and parallel capacitances  $C1, C_{f1}$ , and the primary coil  $L1$ . At the same time, this circuit also includes switches (S4). Switches S7 and S6 are operational at the same time on the secondary side. In order to reach the load, the induced current passes via the secondary coil ( $L2$ ), compensating inductance ( $L_{f2}$ ), series and parallel capacitances ( $C2, C_{f2}$ ), and switches (S7) and (S6). On the battery side of the car, the current moves forward across the load. The corresponding circuit of the bidirectional power transfer system described in Mode I is shown in Figure 4.

**Mode II: ( $0 \leq t \leq \alpha$ )**

The upper switches on the primary side, S1 and S3, are conducting across the time interval  $0$  to  $\alpha$ . However, there is some dead time because the inductance's stored energy is released, which leads to a zero-current condition as the current flows between these two switches. Concurrently, during the same time period on the secondary side, S5 and S7, the higher switches, are conducting. Like the primary side, there is a dead time during which current circulates between switches S5 and S7 as a result of the stored energy in the inductance. Consequently, there is no current flowing through the load [14]. An illustration of the equivalent circuit for the bidirectional power transfer system in operation during Mode II is shown in Figure 5.

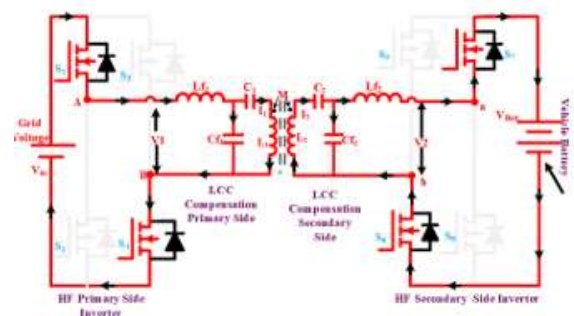


FIGURE 4. Equivalent circuit of presented BWPT operation in Mode I.

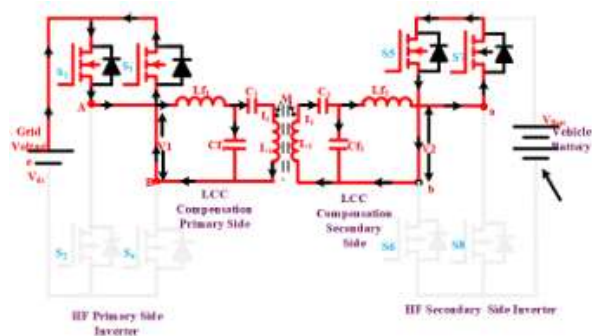


FIGURE 5. Equivalent circuit of presented BWPT operation in Mode II.

**Mode III: ( $\pi + \alpha \leq t \leq 2\pi$ ):**

Switches (S2) and (S3) are operated on the primary side throughout the period ( $\pi + \alpha$  to  $2\pi$ ). Current (I) passes via the primary coil (L1), series and parallel capacitance (C1, Cf1), compensating inductance (Lf1), switches (S2), as well as the switches. At the same time, switches (S8) and (S5) are conducting on the secondary side.

The secondary coil (L2), compensating inductance (Lf2), series and parallel capacitances (C2, Cf2), switches (S8), load, and switches (S5) are all where the induced current passes.

On the vehicle's battery side, the current flows through the load in the opposite direction. The Mode III equivalent circuit operation is shown in Figure 6.

**Mode IV: ( $t \leq \pi + \alpha \leq \pi$ )**

The lower switches (S2) and (S4) on the primary side are conducting during the time interval ( $\pi$  to  $\pi + \alpha$ ).

Nevertheless, some dead time happens as a result of the inductance's stored energy being released, which causes current to circulate.

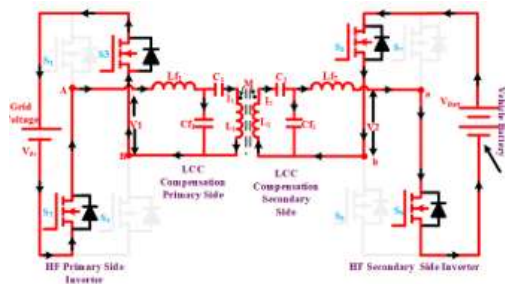


FIGURE 6. Equivalent circuit of presented BWPT operation in Mode III.

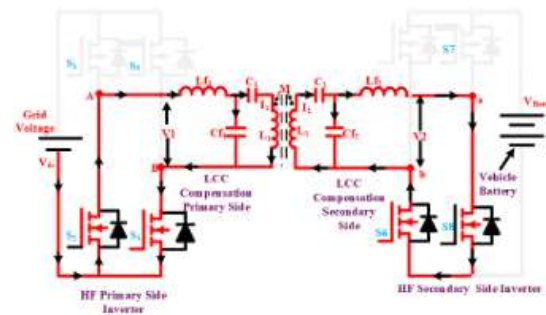


FIGURE 7. Equivalent circuit of presented BWPT operation in Mode IV.

Consequently, the current drops to zero between these two lower switches.

The two lower switches, S6 and S8, are conducting concurrently on the secondary side throughout the same time period. While with the primary side, there is a dead time while current flows between switches S5 and S7, respectively, as the inductance's stored energy is released. Consequently, there is no current flowing over the load. The analogous circuit for the bidirectional power transfer system in Mode IV is shown in Figure 7. Therefore, Figure 8 shows the switching waveforms for several bidirectional wireless power transfer techniques for V2G and G2V operations.

**III. CONTROL OF PHASE SHIFT**

For the primary side circuit to function at the secondary controller's rated current, the value  $\alpha$ —which depends on the reference signal—is essential. It is used to precisely modify the primary side inverter's output voltage.

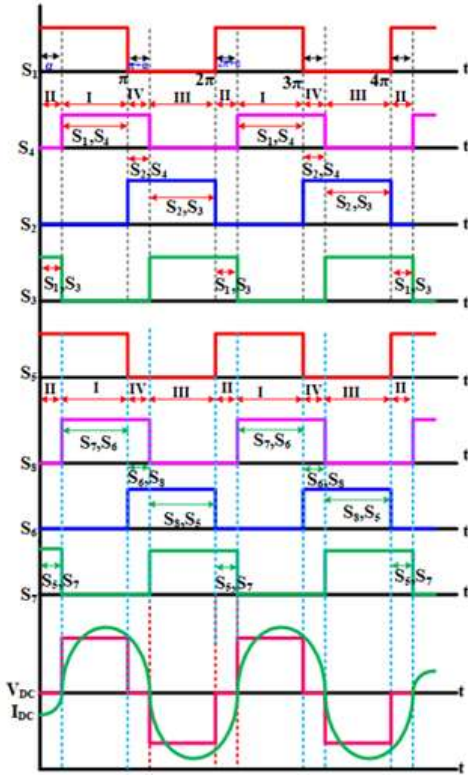


FIGURE 8. Switching waveforms of BWPT for V2G and G2V Operation.

The phase shift ( $\beta$ ) between the secondary inverter's legs is simultaneously generated by the secondary controller, which affects the relationship between the primary and secondary output voltages. Low-level switching signals are used to implement the PWM approach, and these signals are then interpreted for the left and right sides by fine-tuning the phase shift parameters ( $\alpha$ ,  $\beta$ , and  $\delta$ ) [16].

The secondary side control parameters ( $\beta$  and  $\delta$ ) must be changed to achieve the appropriate power flow magnitude and direction. Signals amplified by the driving circuits determine the arrangement of the four switches on either side of the high-frequency converters. These control parameters are essential for modifying the amplitude and phase of the inverter voltages as well as achieving the intended power flow throughout the system [17].

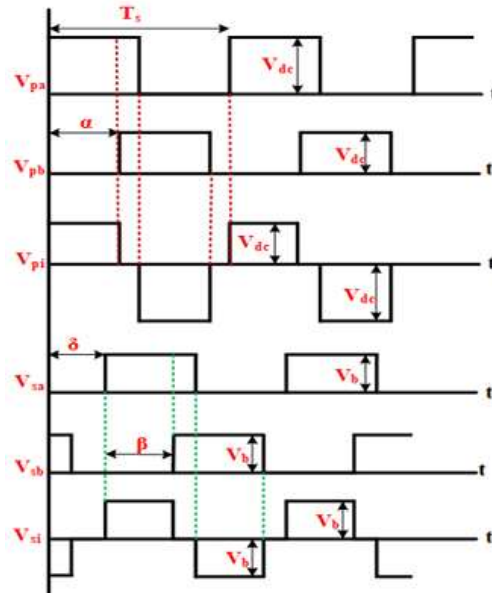


FIGURE9. Switching waveforms of phase angle delay between the two converters.

Every side in BWPT has the ability to act as a load and a supply at the same time. As a result, all parties need to be treated equally. There must be a deliberate lag in the activation of semiconductor switches on both ends in order to engage the full-bridge converters on the primary and secondary sides simultaneously. Phase angles ( $\alpha$ ,  $\beta$ ) and the delay angle ( $\delta$ ) are used to control the power flow between the primary and secondary converters (AC/DC and DC/AC). The switching waveforms and the phase angle delay between the two converters are shown graphically in Figure 9. The power level is usually modulated on both sides by the phase shift angle. The phase difference between the primary and secondary inverters' peak voltages is indicated by the delay angle ( $\delta$ ) [18]. The two converters

The output voltages for the first harmonics,  $V_p(t)$  and  $V_s(t)$ , are written as

$$V_p(t) = \left(\frac{4}{\pi}\right) V_p \sum_{n=1,3}^{\infty} \frac{1}{n} \cos\left(n\omega_r t - \frac{n\alpha}{2}\right) \sin\left(\frac{n\alpha}{2}\right) \tag{1}$$

$$V_s(t) = \left(\frac{4}{\pi}\right) V_p \sum_{n=1,3}^{\infty} \frac{1}{n} \cos\left(n\omega_r t - \frac{n\alpha}{2}\right) \sin\left(\frac{n\beta}{2}\right) \tag{2}$$

where the order of harmonics is denoted by  $n$ . In the equation above,  $\alpha$  and  $\beta$  stand for the phase shift between an inverter pair's switches,  $V_p$  and  $V_s$  for the primary

and secondary side inverter peak voltages, and "n" for the harmonic orders.

#### IV. THE BWPT SYSTEM DESIGN PARAMETERS

For the design of BWPT systems, the phase shift controller with enhanced PFC control must be developed. At the resonance frequency, the power transfer between the primary and secondary coils can be stated.

$$P = \omega 0 M I_p I_s \tag{3}$$

This example shows the mutual inductance between the primary and secondary coils. The letters IP and IS stand for the Root-Mean-Square (RMS) current flowing through the primary and secondary coils, respectively. The mutual inductance between these coils is essential in wireless charging systems since it directly influences the effectiveness and power transfer efficiency. The operating frequency of 85 kHz in this specific situation is in line with the SAEJ2954 standard. The expression for the output power is then as follows:

$$p = 2\pi f 0 (N_p I_p)(N_s I_s) K \sqrt{\hat{L}_p \hat{L}_s} \tag{4}$$

where the operating frequency is denoted by f0. The letters NP and NS stand for main and secondary coil turns, respectively. The inductance return is represented by the symbols ^LP and ^LS for the primary and secondary coils, respectively.

K is a representation of the coupling coefficient between the coils. There will be a smaller air gap if Kislow, and vice versa. The equations determine the mutual inductance per return based on the size and air gap between the charging pads.

$$M = K \sqrt{L_p * L_s} \tag{5}$$

Larger pad diameters and a smaller air gap lead to an increase in mutual inductance (M) [20]. The coupling coefficient (K) rises by 30% to 50% because the ferrite core's self-inductance is almost double that of the air core. [21]. To guarantee that the receiver and transmitter pads are the same size, it is crucial to regulate the output power and ampere-turn ratio. The dimensions of the charging coil and the airgap were used to generate a 3D finite-element analysis (FEA) model with an alumped coil, which computed the coupling coefficient and inductance return. The ampere-turn architecture of the

primary and secondary side coils is still an important design factor for the given size, power rating, and air gap [22]. The LCC compensation provides more design alternatives for current rent and turn configurations than standard series compensation. Figure 2 displays the LCC-LCC compensating circuit layout of a linked coil. The following formula can be used to determine the current IP and IS.

$$I_P = \frac{V_{AB}}{\omega 0 L_{11}}, I_S = \frac{V_{ab}}{\omega 0 L_{22}} \tag{6}$$

According to equation (6), the compensatory inductances L11 and L22 have an impact on the currents IP and IS for the voltage at input-output. A decrease in the coil current IP is made possible by a change in the value of the compensating inductance L11. With LCC-LCC compensation, several coil current ranges (IP) for a given voltage may be found, and the number of turns (NP) can be defined [23]. When an excessive number of turns is chosen to minimize a coil's current, the coil's inductance and the voltage across it notably increase. An very high voltage may raise security and reliability issues due to the insulating layer and turn-to-turn distance of the Litzwire. Furthermore, the maximum voltage of the system may be restricted by certain applications. As a result, the voltage across the coils and capacitor limits the number of spins; equations (7) and (8) can be used to quantitatively depict this relationship.

$$V_{LP} = I_p X_{LP} = j\omega L_p I_p = I_p (2\pi N_p^2 \hat{L}_p) \tag{7}$$

$$V_{LS} = I_s X_{LS} = j\omega L_s I_s = I_s (2\pi N_p^2 \hat{L}_p) \tag{8}$$

The voltage across the coils rises by [2πIpNp^LP] for each consecutive rotation, per the equation above. The following formula is used to determine the input voltage to coil voltage ratio:

$$G_{VP} = \frac{V_{LP}}{V_{AB}} = \frac{X_{LP}}{XL11} = \frac{L_p}{L11} \tag{9}$$

By estimating the resonance frequency, the capacitor value for LCC-LCC correction can be ascertained following coil design and inducer calibration.

$$\omega_0 = \frac{1}{\sqrt{L_{11} C_{11}}} = \frac{1}{\sqrt{(L_p - L_{11}) C_{12}}} \tag{10}$$

$$\omega_0 = \frac{1}{\sqrt{L_{22} C_{22}}} = \frac{1}{\sqrt{(L_s - L_{22}) C_{21}}} \tag{11}$$

Similarly, the pad's design is based on three key elements: the width of the ferrite core to prevent excessive core loss, the number of turns per coil to

accomplish the required self-inductance, and the current rating of each coil, all of which contribute to the Liitzwire gauge. To achieve the standards for capacitor voltage and inductor current, a thorough analysis of electrical, magnetic, and thermal properties is necessary [24]. Use equations (12,13) to depict the currents flowing through the tuning inducers and primary and secondary coils of an LCC-LCC resonant tank.

$$IL_{11} = \frac{MV_{AB}}{\omega 0L_{11}L_{22}}, L_{22} = \frac{MV_{ab}}{\omega 0L_{11}L_{22}} \quad (12)$$

$$IL_{11} = \frac{MV_{AB}}{\omega 0L_{11}}, L_{LS} = \frac{V_{ab}}{\omega 0L_{22}} \quad (13)$$

The voltage ages between the tuning capacitors in LCC-LCC resonance-compensated systems can be computed using equations (14)–(15).

$$V_{C12} = \frac{V_{AB}(L_P - L_{11})}{L_{11}} \quad (14)$$

$$V_{C21} = \frac{V_{AB}(L_S - L_{22})}{L_{22}} \quad (15)$$

Furthermore, the high-frequency high-power capacitor must meet both the voltage and current requirements while taking into account the heating constraints. The actual rated voltages and currents for the proposed design's resotank components are shown in Table 1.

### V. Correction of the Power Factor IN THE BWPT SYSTEM

Power Factor Correction (PFC) can be implemented at the front-end or back-end of an ideal WPT system. But it's important to keep in mind that choosing between front-end and back-end PFC depends on a number of variables, such as system needs, efficiency considerations, and design constraints [25]. Every strategy has pros and cons of its own, and the choice should be based on the particular requirements of the system. In a perfect WPT

TABLE 1.

Electrical circuit parameters of 3.7KW BWPT system.

S: No	Parameters	Symbols	Values
1	Output Power	$P_{out}$	3.7 kW
2	Input AC voltage	$V_{Grid}$	325 V
3	Output Converter Voltage	$V_{out}$	420 V
4	Coupling Co-efficient	$K$	0.4
5	Switching Frequency	$f_s$	85 kHz
6	Mutual Inductance	$M$	46.5 μH
7	Capacitor for Primary Side Series Compensation	$C_p$	31nF
8	Self-Inductance of the Primary Coil	$L_P$	120 μH
9	Secondary Coil Self Inductance	$L_S$	120 μH
10	Secondary Side Series Compensation Capacitor	$C_S$	31nF
11	Capacitance Filter	$C_0$	30 μF

system, the following is an expression for power transmission at the resonance frequency:

$$P_o = \frac{8}{\pi^2} * \frac{V_P * V_S}{\omega * L_M} \quad (16)$$

The interaction between self and mutual inductance can be calculated using the LM, which is calculated using the coupling factor value, the distance between the primary and secondary coils, and the coil misalignment. The letters LP and LS represent the respective self-inductance of the primary and secondary coils. The K value fluctuates primarily in the range of 0.2 to 0.5. The output power can be adjusted using either VP or VS, and the resonance frequency is independent of the load. The automobile SAE standard J2954 describes a frequency spectrum that ranges from 81.39 kHz to 90 kHz. The PFC model includes LCC compensation coupled to an H-bridge converter on both the main and secondary sides, as well as active rectification. Furthermore, the output interfaces for battery charge control have passive DC-DC control. It is believed that power in single-phase alternating current (AC) systems is proportional to the quadratically-sine function, assuming that the unity power factor is corrected.

$$P_g(t) = 2V_g I_g \sin(\omega_g t) \quad (17)$$

where Vg and Ig stand for the grid's input voltage and RMS current, respectively. The switching frequency is not a control variable in this scenario. Therefore, controlling the average low-frequency primary voltage (Vpf) or secondary voltage (Vsf) is how power regulation is achieved. This allows for a 100Hz variable power source while guaranteeing PFC. Thus, the power transfer can be computed as follows:

$$P_g(t) = V_g I_g = P_{mean}(1 + \cos(2\omega_g)) \tag{18}$$

This study makes the assumption that continuous current (CC) and continuous voltage (CV) control cooperate to regulate batteries. We'll use battery current and voltage readings to operate this control mechanism. In order to assist with CC management,

Additionally, a current saturation mechanism has been incorporated. The internal current control loop, which effectively counteracts both internal and external disturbances, becomes essential to the regulation of the accurate current. The transmitted power can be calculated as follows since the secondary-side voltage and the resonant current are always in line.

$$p = \frac{P_{mean}^* M \omega_0 \pi}{2V_{BAT}} = \frac{4}{\pi \omega_0 i \hat{p}} \tag{19}$$

where  $\hat{V}_{pf}$  and  $\hat{V}_{sf}$ , respectively, represent the fundamental voltage amplitudes on the main and secondary sides at the switching frequency.

$$\hat{V}_{Pf} = \frac{4}{\pi} V_r \sin(\delta_p \pi / 2) \tag{20}$$

$$\hat{V}_{Pf} = \frac{4}{\pi} V_{BAT} \sin(\delta_s \pi / 2) \tag{21}$$

where the primary and secondary duty cycles are denoted by  $\delta_p$  and  $\delta_s$ , respectively.  $V_{BAT}$  is the battery voltage, and  $V_r$  is the rectified grid voltage. Both PFC control techniques require a grid-connected unfolding 50 Hz active rectifier, regardless of the converter that performs PFC and current shaping.

By adjusting unregulated (AC) voltage, resonant inverters regulate the primary resonant tank (VP) and the current flow between the primary and secondary coils. Furthermore, when an off-board primary-side resonant inverter manages the power control, communication systems or estimate techniques are required.

## VI. OUTCOMES AND TALK

According to the specifications listed in Table 1, a simulation analysis and experimental verifications are conducted for the proposed system's 3.7 kW power rating. For both the G2V and V2G modes of operation, the MATLAB simulation is run. Important characteristics are measured, including the grid side voltage and current, the transmitter and reception coil sides, and the inverter end. The output voltage at the secondary inverter side ( $V_{out}$ ) is 420V, and the input AC

voltage ( $V_{Grid}$ ) is 325V. These simulation settings are in accordance with the guidelines provided. Consideration is given to an 85 kHz switching frequency ( $f_s$ ) and a coupling coefficient ( $K$ ) of 0.4. The parts of the system include of the subsequent parts: the primary coil's self-inductance ( $L_P$ ), the secondary coil's self-inductance ( $L_S$ ), the secondary side series compensation capacitor ( $C_S$ ), the capacitance filter ( $C_0$ ), and the primary side series compensation capacitor ( $C_P$ ). It is believed that the mutual inductance ( $M$ ) is 46.5 $\mu$ H. This comprehensive simulation study ensures a thorough analysis of the performance of the proposed dual-phase shift Pulse Width Modulation (PWM) technique under varied operating circumstances.

### A. G2V SIDE SIMULATION RESULTS

First, the G2V operational simulation mode is used, taking into account a grid frequency of 50 Hz and a grid supply voltage magnitude of 325V. The nominal grid input voltages' sinusoidal change is depicted in Figure 16(a).

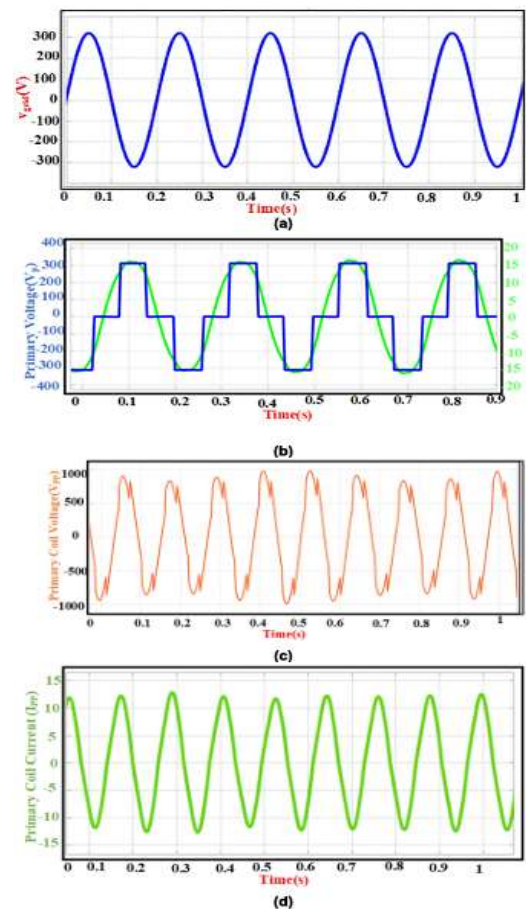


FIGURE 16. (a)The Grid Input Voltage (b) Primary side Converter voltage control ( $V_{pp}$ ) Current ( $I_{pp}$ ) (c) Primary coil voltage ( $V_{pp}$ ) across the transmitter pads

(Vpp) (d) The Primary coil current across the transmitter pads (Ipp).

The voltage and current of the primary side converter are shown in

The waveform in Figure 16(b) shows that the THD is lower when operating in the G2V mode with primary side control. On the other hand, the voltage and primary coil current plotted

Figure 16(c) and (d) demonstrate that voltage harmonics are present.

On the other hand, the modulated current (Ipp) is 12A and the modulated voltage (Vpp) is nearly 940 V on the primary coil side. On the other hand, Figure 17(a) displays the secondary side voltage and current, which are 220V and 18A, respectively, due to unregulated secondary side regulation. In the same way, the secondary coil side modulated current (Iss) is 8 A, and the secondary coil side modulated voltage (Vss) is 1000V. The secondary side waveform shows that there are more voltage harmonics present than current.

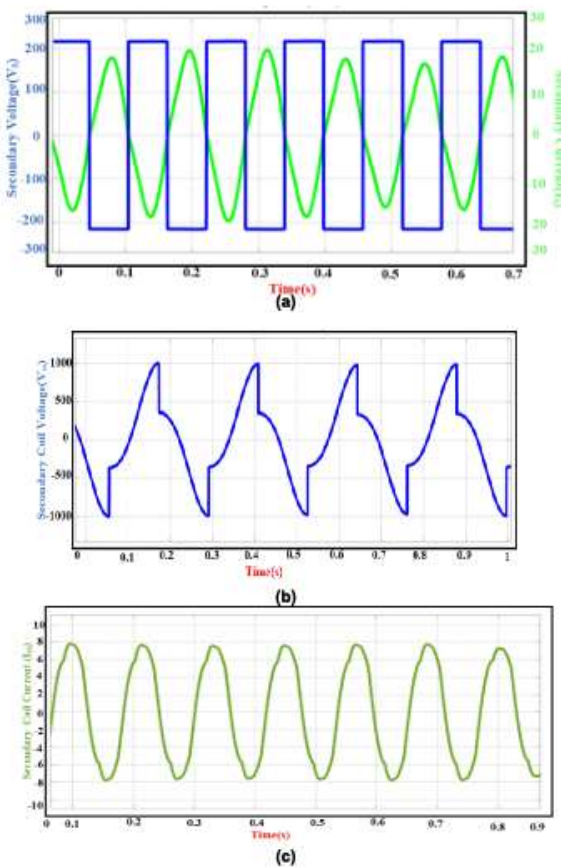


FIGURE 17. (a) Secondary side Converters voltage control (Vss) Current (Iss) Waveforms (b) Secondary

coil voltage (Vss) across the Receiver pads (c) Secondary coil Current (Iss) across the Receiver pads. the coil end's harmonic level. Additionally, the compensating resonance capacitance at the secondary converter's output reduces the THD level.

The primary side control offers superior control over the THD and bifurcation at the primary and secondary ends, according to the simulation research results for the G2V operation. Conversely, the same PFC is brought about during G2V operation by the utilization of unregulated operation at the secondary side.

When using the V2G operation for secondary control, the improvement in the PFC was visible.

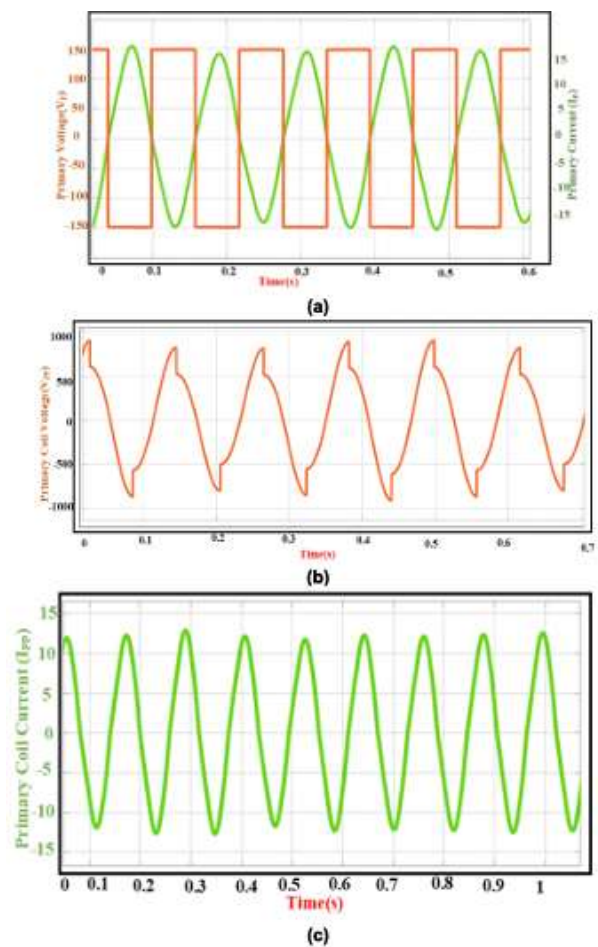


Fig. 18. Current (Ipp) at the primary side, converter voltage (Vpp), voltage (Vpp) across the primary pads, and primary coil current (Ipp) are the first three variables.

**B. V2G SIDE SIMULATION RESULTS** The secondary converter is controlled during the V2G portion of the simulation research, and the primary side

converter is not modulated. With the exception of the control flow modifications, the design parameters are the same for the G2V operation. The voltage and current of the primary side unregulated square-wave modulation converter are displayed in Figure 18(a).

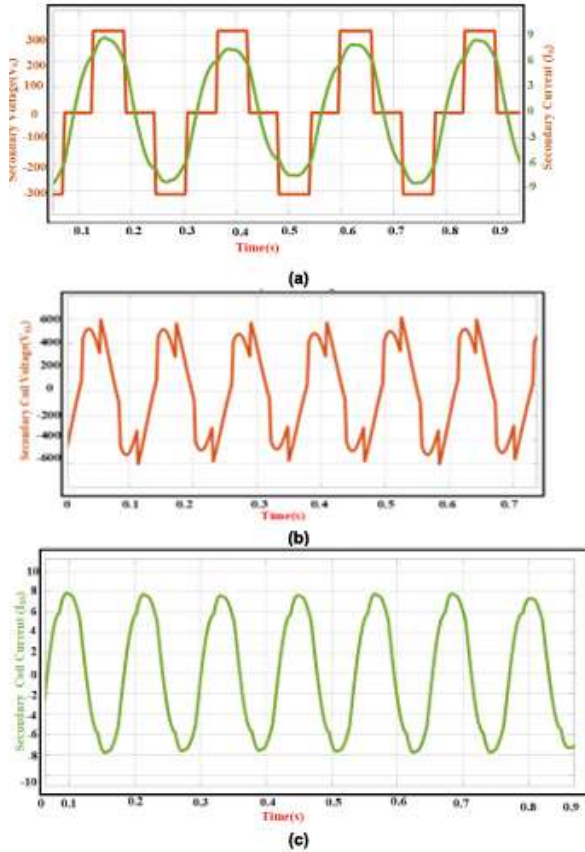


FIGURE 19. (a) Secondary side Converter voltage control (Vss) Current (Iss) (b) Secondary side coil voltage (Vss) across the Receiver Pads (c) Secondary side coil Current (Iss) across the Receiver Pad.

The principal current ( $I_{pp}$ ) and primary side voltage ( $V_{pp}$ ) have peak values of 10 A and 150 V, respectively. In the meantime, the sinusoidal current is displayed in Figures 18(b) and 18(c) and fluctuating voltage that comes from the voltage and current of the primary side pad. In comparison to the voltage, the primary side has the lowest current THD. Additionally, in V2G mode of operation, the PFC at the main side with secondary end control is improved. fluctuating voltage that comes from the voltage and current of the primary side pad. In comparison to the voltage, the primary side has the lowest current THD. Additionally, in V2G mode of operation, the PFC at the main side with secondary end control is improved.

Figure 19(a) through 19(c) show the secondary side measured parameters. The secondary side converter voltage and current, with amplitudes of 310 V and 8 A, are displayed in Figure 19(a). Likewise, Figure 19(b) and Figure 19(c) show the secondary side coil voltage and current. The coil's voltage and current are 600V and 8A, respectively. The enhanced PFC over the primary side control is demonstrated by the secondary side control operating in the V2G mode. In contrast, the bifurcation and THD remain unaltered in V2G mode.

### C. G2V Operation with ANN-Enhanced Control

First, the **Grid-to-Vehicle (G2V)** operational simulation mode is executed with a grid frequency of **50 Hz** and a grid supply voltage magnitude of **325 V**. The sinusoidal nature of the nominal grid input voltage is illustrated in **Figure 20(a)**. The voltage and current waveforms of the **primary side converter** under control are depicted in **Figure 20(b)**, showing a notably **lower Total Harmonic Distortion (THD)** when operating in G2V mode with primary side control.

However, **Figures 20(c) and 20(d)**, which display the voltage and current across the **primary coil**, reveal the presence of voltage harmonics in the system. In this configuration, the **modulated current ( $I_{pp}$ )** on the primary coil reaches approximately **12 A**, while the **modulated voltage ( $V_{pp}$ )** is close to **940 V**.

On the **secondary side**, **Figure 21(a)** presents the voltage and current waveforms, indicating values of **220 V** and **18 A**, respectively. This is a result of **unregulated control on the secondary side**, which introduces more pronounced voltage harmonics. Additionally, the **modulated current ( $I_{ss}$ )** at the secondary coil is **8 A**, and the **modulated voltage ( $V_{ss}$ )** reaches **1000 V**, as shown in **Figures 21(b) and 21(c)**. The waveform characteristics confirm that **voltage harmonics dominate over current harmonics** at the secondary coil end. However, the inclusion of **compensating resonance capacitance** at the secondary converter's output contributes to a **reduction in THD** levels.

The simulation results clearly demonstrate that **primary side control** yields **superior management of THD and bifurcation phenomena** across both the primary and

secondary sides during G2V operation. This improvement is evident even when the secondary side remains unregulated, which also contributes to maintaining a relatively stable **Power Factor Correction (PFC)**.

To further enhance control precision and harmonic suppression, an **Artificial Neural Network (ANN)**-based controller is integrated into the system. The ANN dynamically learns and adjusts control parameters in real-time by analyzing grid and load conditions, which allows for **optimized pulse-width modulation** and **adaptive compensation strategies**. Under ANN-

assisted control, the system shows **greater resilience to voltage fluctuations, reduced bifurcation effects, and more efficient harmonic mitigation**—especially during mode transitions and load disturbances.

In contrast, during **Vehicle-to-Grid (V2G)** operation with **secondary-side control**, simulation results indicate visible improvements in **PFC** when ANN-based modulation is employed. This enhancement further confirms that ANN-supported dual-phase PWM control can **dynamically optimize bidirectional power flow**, ensuring **high efficiency, low harmonic distortion, and stable operation** in both G2V and V2G modes.

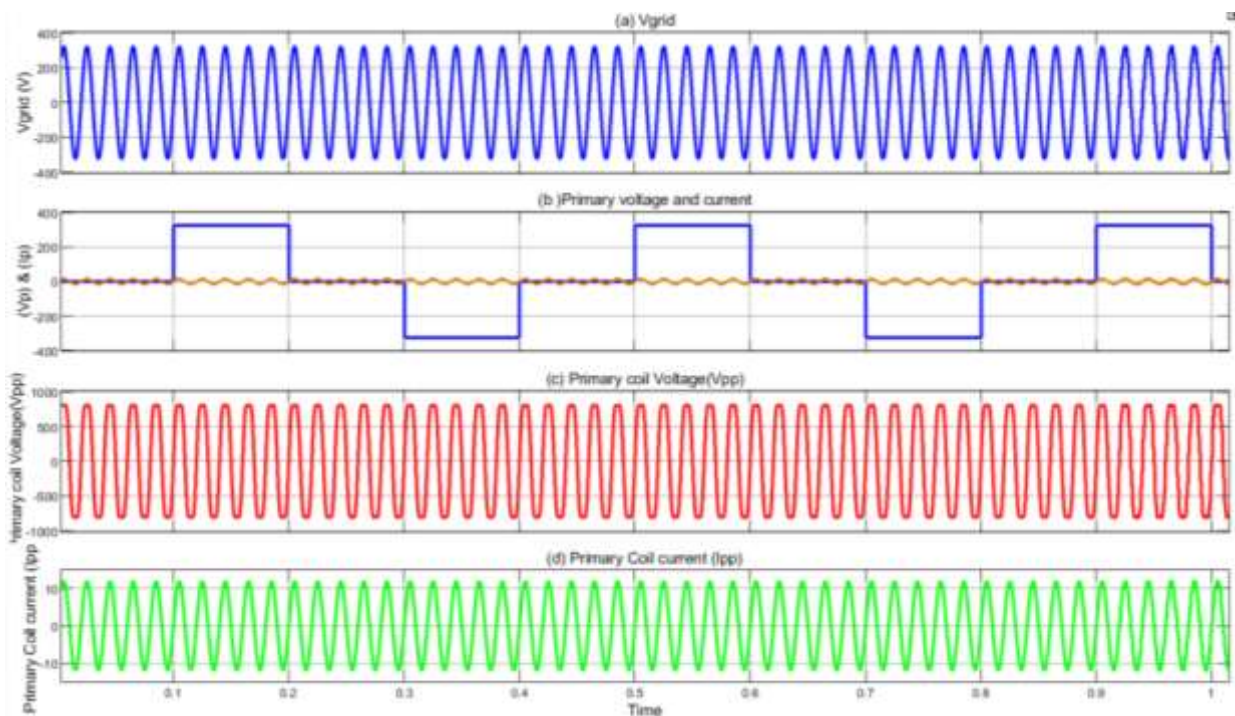


FIGURE 20. (a) Grid input voltage waveform (50 Hz, 325 V RMS) under ANN-based control. (b) Primary-side converter voltage ( $V_{pp}$ ) and current ( $I_{pp}$ ) with ANN-optimized dual-phase PWM, showing reduced THD. (c) Primary coil voltage ( $V_{pp}$ ) across transmitter pads with improved harmonic suppression. (d) Primary coil current ( $I_{pp}$ ) under ANN control, highlighting stable waveform and enhanced power factor.

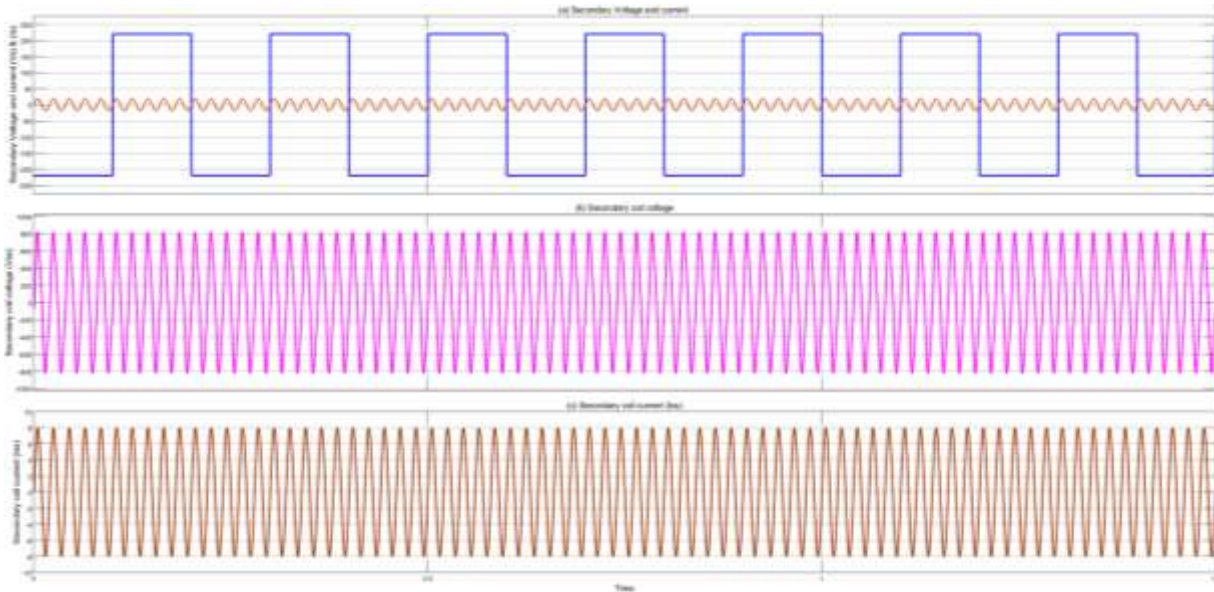


FIGURE 21. (a) Secondary-side converter voltage ( $V_{ss}$ ) and current ( $I_{ss}$ ) waveforms under unregulated control, with ANN-assisted system monitoring. (b) Secondary coil voltage ( $V_{ss}$ ) across receiver pads, showing voltage harmonics. (c) Secondary coil current ( $I_{ss}$ ) across receiver pads, with ANN aiding in THD reduction via adaptive resonance compensation.

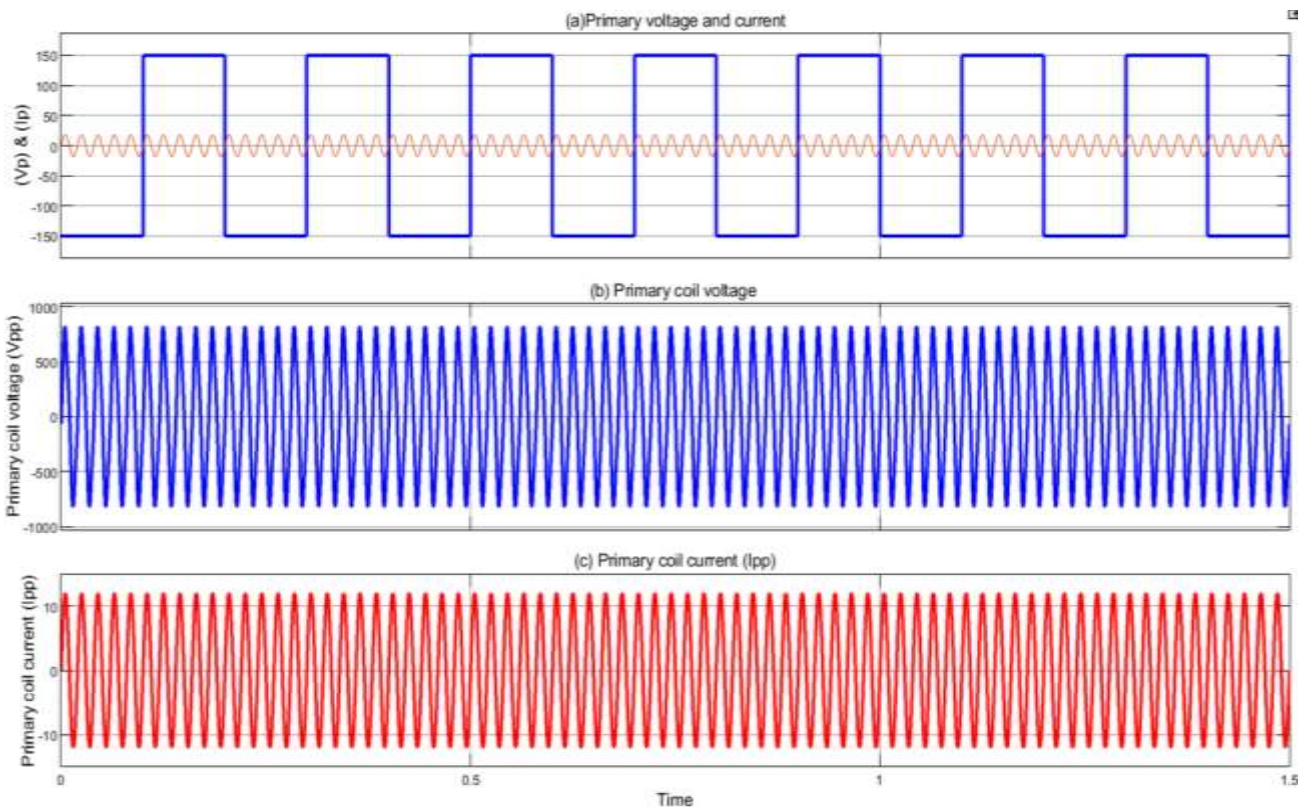
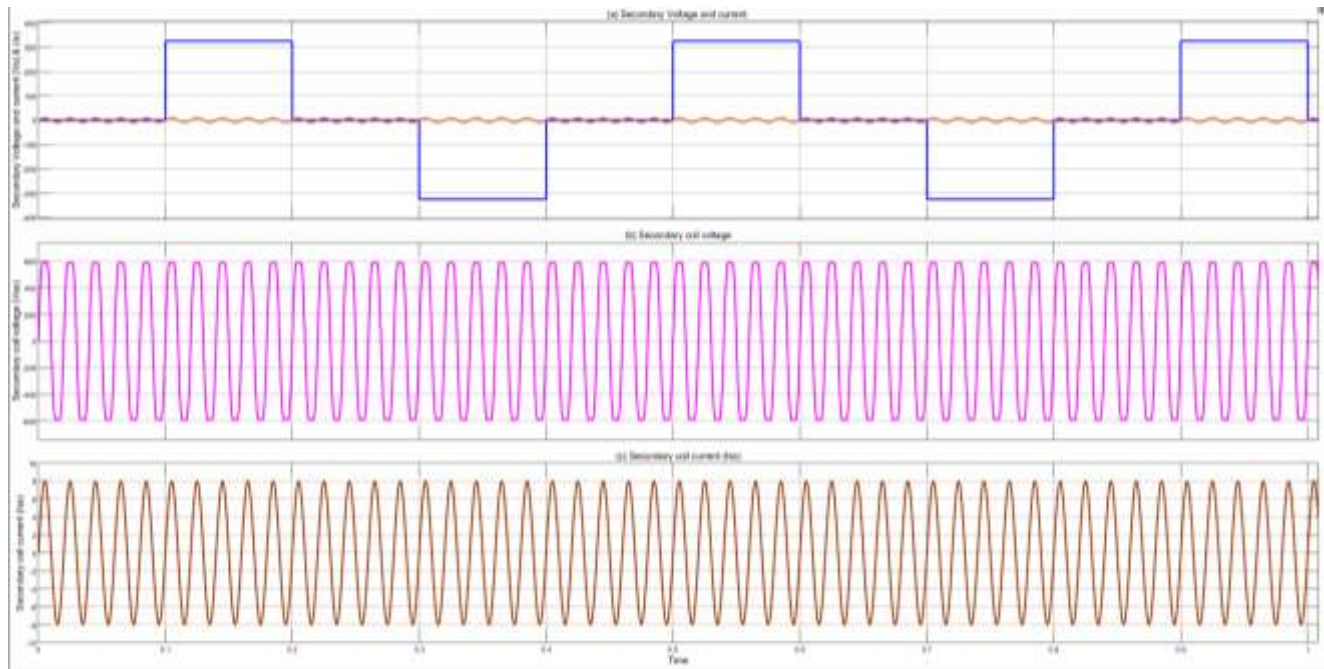
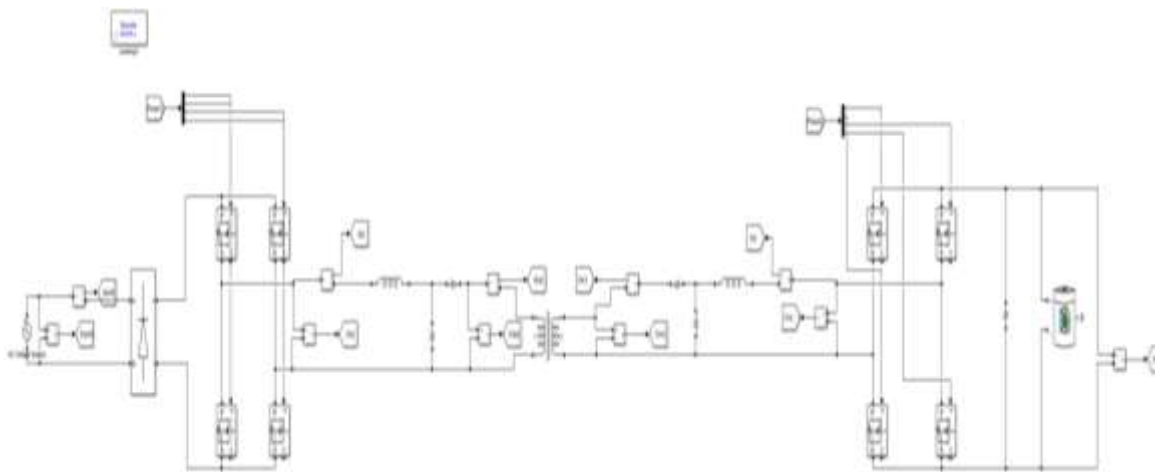


FIGURE 22. (a) Primary-side unregulated converter voltage ( $V_{pp}$ ) and current ( $I_{pp}$ ) under square-wave modulation in V2G mode. (b) Voltage ( $V_{pp}$ ) across primary transmission pads. (c) Primary coil current ( $I_{pp}$ ) under ANN-monitored secondary-side control, showing reduced THD in current



**FIGURE 23.** (a) Secondary-side converter voltage ( $V_{ss}$ ) and current ( $I_{ss}$ ) under ANN-optimized V2G control. (b) Secondary coil voltage ( $V_{ss}$ ) across receiver pads. (c) Secondary coil current ( $I_{ss}$ ), with ANN ensuring waveform stability and improved PFC.



**Figure 24.** V2G and G2V circuit diagram

**D. V2G Operation with ANN-Enhanced Control**

During the **Vehicle-to-Grid (V2G)** operation, control is shifted to the **secondary converter**, while the **primary side converter operates in unmodulated square-wave mode**. Apart from this change in control strategy, the design parameters remain consistent with those used in G2V mode.

The **primary side voltage ( $V_{pp}$ )** and **current ( $I_{pp}$ )** waveforms under unregulated operation are shown in

**Figure 22(a)**, with observed peak values of **150 V** and **10 A**, respectively. The current waveform maintains a more **sinusoidal nature** compared to the voltage, as seen in **Figures 22(b) and 22(c)**, which represent the **voltage and current across the primary pad**. Under this configuration, the **current THD is lower than the voltage THD**, highlighting the natural smoothing effect due to inductive coupling.

The integration of an **Artificial Neural Network (ANN)** enhances real-time signal tracking and predictive

adjustment at the secondary side. As a result, the system dynamically improves **power factor correction (PFC)** on the **primary side**, even when control originates from the secondary end. The ANN adapts to varying load and grid conditions, ensuring **stable power flow**, improved **converter synchronization**, and **reduced control delays**.

On the **secondary side**, the **converter voltage and current** are presented in **Figure 23(a)**, with measured amplitudes of **310 V** and **8 A**, respectively. The **coil-side voltage and current**, shown in **Figures 23(b) and 23(c)**, reach **600 V** and **8 A**. ANN-based control further **optimizes secondary-side modulation**, maintaining **stable operation** while effectively managing **voltage harmonics**.

Although **bifurcation and THD** are not significantly altered in V2G mode, the **ANN-enhanced control** contributes to a more consistent PFC, **mitigates transient instability**, and ensures efficient bidirectional energy exchange.

## VII. ANALYZATION

The suggested work provides an appropriate method for addressing issues that come up in BWPT systems used for EV charging. The proposed dual-phase shift-regulated PWM methodology offers an advanced power factor control strategy intended for two-way operations, surpassing the limitations of conventional power factor control techniques. To support the efficacy of the suggested system, a comprehensive study is carried out, accounting for elements including power factor, bifurcation, total harmonic distortion (THD), and power losses. Simulation and experimental validation evaluations for G2V and V2G modes show power transfer efficiencies of 94.4% and 90.1%, respectively, for a 3.7 kW power rating at an operating frequency of 85 kHz. The mode of V2G of operation with dual phase shift control provides improved power factor management without altering the bifurcation factor and THD. On the other hand, the THD and bifurcation are improved by the G2V mode of operation with the primary control. This study highlights that enhancing control mechanisms is essential to the creation of intelligent and sustainable energy systems. It not only facilitates the integration of EVs into smart grids but also raises the general effectiveness of BWPT systems. Future studies in BWPT systems focus on enhancing the

scalability and adaptability of the proposed dual-phase shift Pulse Width Modulation (PWM) technology to accommodate various power ratings and frequencies. Analyzing the integration of innovative Artificial intelligence and machine learning are two examples of technologies that could aid in improving control strategies for increased system performance and efficiency. Additionally, looking into the potential integration of energy storage devices into the System reliability and grid stability may be enhanced by a bidirectional power transmission arrangement.

## REFERENCES

- [1] M. Venkatesan, N. Rajamanickam, P. Vishnuram, M. Bajaj, V. Blazek, L. Prokop, and S. Misak, "A Review of compensation topologies and control techniques of bidirectional wireless power transfer systems for electric vehicle applications," *Energies*, vol. 15, no. 20, Oct. 1, 2022, doi: 10.3390/en15207816.
- [2] Q. He, Q. Luo, K. Ma, P. Sun, and L. Zhou, "Analysis and design of a single-stage bridgeless high-frequency resonant AC/AC converter," *IEEE Trans. Power Electron.*, vol. 34, no. 1, pp. 700–711, Jan. 2019.
- [3] M. Kim, D.-M. Joo, and B. K. Lee, "Design and control of inductive power transfer system for electric vehicles considering wide variation of output voltage and coupling coefficient," *IEEE Trans. Power Electron.*, vol. 34, no. 2, pp. 1197–1208, Feb. 2019, doi: 10.1109/TPEL.2018.2835161.
- [4] X. Wang, J. Xu, M. Leng, H. Ma, and S. He, "A hybrid control strategy of LCC-S compensated WPT system for wide output voltage and ZVS range with minimized reactive current," *IEEE Trans. Ind. Electron.*, vol. 68, no. 9, pp. 7908–7920, Sep. 2021, doi: 10.1109/TIE.2020.3013788.
- [5] X. Qu, H. Chu, S.-C. Wong, and C. K. Tse, "An IPT battery charger with near unity power factor and load-independent constant output combating design constraints of input voltage and transformer parameters," *IEEE Trans. Power Electron.*, vol. 34, no. 8, pp. 7719–7727, Aug. 2019, doi: 10.1109/TPEL.2018.2881207.
- [6] X. Liu, N. Jin, X. Yang, K. Hashmi, D. Ma, and H. Tang, "A novel single switch phase controlled wireless

power transfer system,” *Electronics*, vol. 7, no. 11, p. 281, Oct. 2018, doi: 10.3390/electronics7110281.

[7] V. Shevchenko, O. Husev, R. Strzelecki, B. Pakhaliuk, N. Poliakov, and N. Strzelecka, “Compensation topologies in IPT systems: Standards, requirements, classification, analysis, comparison and application,” *IEEE Access*, vol. 7, pp. 120559–120580, 2019.

[8] D. Xu, C. Zhao, and H. Fan, “A PWM plus phase-shift control bidirectional DC–DC converter,” *IEEE Trans. Power Electron.*, vol. 19, no. 3, pp. 666–675, May 2004, doi: 10.1109/TPEL.2004.826485. [9] R. Bosshard, J. W. Kolar, J. Mühlethaler, I. Stevanovic, B. Wunsch, and F. Canales, “Modeling and  $\eta$ – $\alpha$ -Pareto optimization of inductive power transfer coils for electric vehicles,” *IEEE J. Emerg. Sel. Topics Power Electron.*, vol. 3, no. 1, pp. 50–64, Mar. 2015, doi: 10.1109/JESTPE.2014.2311302.

[10] R. Bosshard and J. W. Kolar, “Inductive power transfer for electric vehicle charging: Technical challenges and tradeoffs,” *IEEE Power Electron. Mag.*, vol. 3, no. 3, pp. 22–30, Sep. 2016, doi: 10.1109/MPEL.2016.2583839.

[11] M. Neath, “Bidirectional inductive power transfer system: Analysis and control,” Ph.D. dissertation, Univ. Auckland, Auckland, New Zealand, 2013. [Online]. Available: <http://hdl.handle.net/2292/22756>